

# Axial perturbations of hairy black holes in generalised scalar-tensor theories

Georgios Antoniou,<sup>1,2</sup> Caio F. B. Macedo,<sup>3</sup> Andrea Maselli,<sup>4</sup> and Thomas P. Sotiriou<sup>5,6</sup>

<sup>1</sup>*Dipartimento di Fisica, “Sapienza” Università di Roma & Sezione INFN Roma1, P.A. Moro 5, 00185, Roma, Italy*

<sup>2</sup>*Dipartimento di Fisica, Università di Pisa, 56127 Pisa, Italy*

<sup>3</sup>*Faculdade de Física, Universidade Federal do Pará, Salinópolis, Pará, 68721-000 Brazil*

<sup>4</sup>*Gran Sasso Science Institute (GSSI), I-67100 L’Aquila, Italy*

<sup>5</sup>*Nottingham Centre of Gravity & School of Mathematical Sciences, University of Nottingham, University Park, Nottingham NG7 2RD, United Kingdom*

<sup>6</sup>*School of Physics and Astronomy, University of Nottingham, University Park, Nottingham NG7 2RD, United Kingdom*

Gravitational wave observations can test the validity of General Relativity (GR) in the strong field regime. Certain classes of scalar-tensor theories indeed predict that compact objects can exhibit significant deviations from their GR counterparts. Here we explore the quasinormal modes of axial perturbations in spherically symmetric black holes in three such classes: (i) dilatonic black holes with an additional scalar-Ricci coupling (EdRGB), (ii) spontaneously scalarized black holes (EsRGB) with a quadratic coupling to the Gauss-Bonnet invariant and the Ricci scalar, (iii) spontaneously scalarized black holes with a quadratic and a quartic coupling to the Gauss-Bonnet invariant.

## I. INTRODUCTION

The first detection of gravitational waves [1] marked the beginning of gravitational-wave-astronomy. We already have an impressive number of observations at hand [1–5], which is expected to grow significantly by the time the 4th observational run has concluded, with KAGRA now joining the LIGO and VIRGO collaborations. This unprecedented access to the strong-field regime of gravitation allows us to confront potential deviations from GR manifesting in these high curvature regions, and to test the existence of additional fields.

A scalar field nonminimally coupled to gravity would be perhaps the simplest example of a new field that leads to a modification of GR. In recent years, various black hole solutions have been derived in the context of scalar-Gauss-Bonnet gravity, where a scalar couples to the Gauss-Bonnet curvature invariant. These theories constitute sub-classes of more general scalar-tensor theories belonging in the Horndeski framework [6–8]. Scalar-Gauss-Bonnet gravity exhibits significant deviations from GR in the strong gravitational field regimes, while passing high accuracy tests of GR in the weak-field approximation [9]. In particular, black holes in scalar-Gauss-Bonnet gravity evade no-hair theorems [10–13] and can carry scalar-hair [13–18], which is sourced by the nontrivial interactions of the scalar field with the Gauss-Bonnet invariant.

Different types of couplings between the scalar and the Gauss-Bonnet invariant allow for black holes with different characteristics. For linear coupling all black holes will have scalar hair. This coupling is known to be the only shift-symmetric interaction that can lead to black hole hair [16, 19], which is particularly relevant for massless (or almost massless) fields. However, it can also be thought of as the weak field or weak coupling limit of the exponential coupling, which arises as a limit of heterotic string theory, and has received a lot of attention in the context of black holes [14, 15, 20, 21]. A quadratic

coupling, or more general couplings that allow for GR solutions, can instead lead to black hole scalarization: whether black holes will have hair or not depends on their mass [13, 18] or spin [22].

An important feature of models that exhibit black hole scalarization, is that only a few interaction terms that appear in linear perturbation theory around GR determine whether scalarization occurs [23], whereas the properties of scalarized black hole solution are very sensitive to the specific nonlinear interaction included in the model [24–28]. Hence, the viability of such models depends crucially on the type of nonlinear interactions that are present. There has been a considerable amount of work on all aspects of theories that exhibit scalarization and of scalarized black holes, including static and spinning solutions [13–15, 28–30], their stability [24–26, 31–34], observational imprints [35], as well as determining whether they can be simulated in the context of a well-posed initial value problem with numerical relativity techniques [36–38]. See also Ref. [39] for a review.

One particular interaction, namely a coupling between the scalar field and the Ricci curvature, has been shown to improve the behaviour and properties of scalarization models and their black holes on multiple counts. It stabilizes otherwise unstable scalarized black hole solutions [28]; it prevents neutron stars from scalarizing [40], thereby removing pulsar constraints; it allows for a late-time GR cosmological attractor [41], thereby making scalarization cosmologically viable; it improves the hyperbolicity of the linear perturbation equations [28] and mitigates the loss of hyperbolicity in spherical collapse [42]. It is therefore particularly interesting to study quasi-normal modes (QNMs) for black holes in theories that contain this interaction.

The QNM spectrum of dilatonic black holes has been studied in [43, 44] and in [45] for static and slowly rotating solutions, respectively. In such works the Einstein-Hilbert action is supplemented by the scalar-GB interaction and a canonical kinetic term for the scalar. Polar and

axial perturbations have also been studied in the context of spontaneous scalarization with a quadratic exponential coupling in [33, 46]. Here we will consider an action that contains couplings of the scalar to both the Gauss-Bonnet invariant and the Ricci scalar. This generalizes earlier work and will allow us to analyse the effects of the Ricci coupling to the QNMs for the first time.

The paper is structured as follows: in Sec. II we introduce the theoretical framework of our analysis, containing the dilatonic and spontaneously scalarized black holes as special cases. In Sec. III we discuss the numerical background solutions emerging in this framework, and we introduce linear order axial perturbations. We present the axial potential and discuss two different methods of searching for the QNMs, namely integration in the time and frequency domains. In Sec. IV we present the main results of our analysis. Finally, in Sec. V we present our conclusions.

## II. THEORETICAL SETUP

We consider the following theory

$$S = \frac{1}{2\kappa} \int d^4x \sqrt{-g} \left[ R + X + J(\phi)R + F(\phi)\mathcal{G} \right], \quad (1)$$

where  $\kappa = 8\pi G$ ,  $X = -(\nabla\phi)^2/2$  is the scalar-field kinetic term, and  $\mathcal{G} \equiv R_{\mu\nu\rho\sigma}R^{\mu\nu\rho\sigma} - 4R_{\mu\nu}R^{\mu\nu} + R^2$  is the Gauss-Bonnet invariant. The field equations for the metric and for the scalar field obtained by varying the action are given by:

$$\begin{aligned} & [1 + J(\phi)]G_{\mu\nu} + \frac{1}{4}g_{\mu\nu}(\nabla\phi)^2 - \frac{1}{2}\nabla_\mu\phi\nabla_\nu\phi \\ & + (g_{\mu\nu}\nabla^2 - \nabla_\mu\nabla_\nu)J(\phi) \\ & + \frac{1}{g}g_{\mu(\rho}g_{\sigma)\nu}\epsilon^{\kappa\rho\alpha\beta}\epsilon^{\sigma\gamma\lambda\tau}R_{\lambda\tau\alpha\beta}\nabla_\gamma\nabla_\kappa F(\phi) = 0, \end{aligned} \quad (2)$$

and

$$\nabla_\mu\nabla^\mu\phi + (\partial_\phi J)R + (\partial_\phi F)\mathcal{G} = 0, \quad (3)$$

where  $\partial_\phi$  denotes derivatives with respect to  $\phi$ .

Although the action we are considering is not a complete effective field theory (EFT), it arguably contains the most interesting terms for strong field phenomenology in such an EFT. As already discussed in the introduction, the coupling between the scalar and the Gauss-Bonnet invariant leads to hairy black holes [13, 15, 17, 18, 22, 24–27, 30, 47–54]. The coupling with the Ricci scalar does not generate hairy solutions but it modifies the properties of the ones obtained from the Gauss-Bonnet coupling [28, 40–42]. These two couplings could also be considered responsible for breaking shift symmetry for the scalar in curved spacetimes.

Action (1) covers a very large theory space so in practice we focus on specific interesting sections of it:

### 1. Einstein-dilaton-Ricci-Gauss-Bonnet

**(EdRGB).** This case corresponds to the coupling functions  $J(\phi) = -\beta\phi^2/4$  and  $F(\phi) = \alpha\exp(\phi)/4$ . The BHs belonging to this family have secondary hair. In absence of the coupling with the Ricci term, i.e.  $\beta \rightarrow 0$ , the theory reduces to that of EdGB dilatonic black holes which are often viewed as a low-energy limit of some string theory [15].

### 2. Einstein-scalar-Ricci-Gauss-Bonnet

**(EsRGB).** This case corresponds to choosing coupling functions  $J(\phi) = \beta\phi^2/4$  and  $F(\phi) = \alpha\phi^2/2$ . This choice leads to scalarized black hole solutions. Their properties and radial stability have been studied in [27, 28], where it was shown that the Ricci term can stabilize the otherwise unstable solutions when  $\beta > 0$ .

### 3. Einstein-scalar-Gauss-Bonnet

**(EsGB):** This case corresponds to the choice  $J(\phi) = 0$  and  $F(\phi) = \alpha\phi^2/2 + \zeta\phi^4/4$ . We consider it to explore the minimum requirements to generate stable spontaneously scalarized BHs with only the Gauss-Bonnet term. While the quadratic term is enough to spontaneously scalarize BHs, these scalarized black holes would be radially unstable [24], and the quartic term in the coupling can render them stable [25].

The key difference between the first and the other two cases we consider is that in EdRGB gravity all black holes will carry scalar hair, whereas EsRGB and EsGB gravity exhibit spontaneous scalarization and only certain black holes will have hair. We can describe the main idea behind spontaneous scalarization as follows. Let us consider a BH solution in GR, and compute linear radial perturbation of the scalar field around its constant background value  $\phi_0$ , i.e.  $\phi = \phi_0(r) + \delta\phi(t, r, \theta, \varphi)$ . Then, from the field equation (3) we have

$$\square\delta\phi = -[\partial_\phi^2 J R + \partial_\phi^2 F \mathcal{G}]_{\phi=\phi_0} \delta\phi, \quad (4)$$

where the quantity in square brackets acts as an effective mass (squared)  $m_{\text{eff}}^2$  for  $\phi$ . In this framework GR solutions are possible provided that  $\phi_0$  exists and that  $\partial_\phi F|_{\phi=\phi_0} = 0$ , with  $\partial_\phi^2 F|_{\phi=\phi_0} \mathcal{G} < 0$ . However, if the effective mass becomes sufficiently negative (after appropriately fixing the sign of the coupling function), it can trigger a tachyonic instability leading to spontaneously scalarised BH solutions, which branch out from the GR limit.

By studying the linear stability of scalar perturbations around the GR background, we can find a threshold value for the constant  $\alpha = \alpha_t$ . We may decompose the scalar perturbations in spherical harmonics  $\delta\phi \sim e^{-i\omega t} \phi_1(r) Y_\ell^m(\cos\theta) e^{-im\varphi}/r$ . This allows us to look for instabilities which will grow and eventually lead to the development of scalar hair. These unstable states correspond to solutions of the scalar perturbation equation.

	Threshold $\alpha_t/M^2$		
	$\ell = 0$	$\ell = 1$	$\ell = 2$
$n = 0$	0.719	2.088	4.098
$n = 1$	4.960	7.589	10.96
$n = 2$	13.03	16.94	21.63

TABLE I. Scalarization threshold for various pairs  $(n, \ell)$ .

for which  $d\phi_1/dr|_{r \rightarrow \infty} = 0$ . The perturbation equation on a Schwarzschild background reads

$$r(r-r_h)\phi_1'' + r_h\phi_1' + \left[ \frac{\omega^2 r^3}{r-r_h} + \frac{12\alpha r_h^2}{r^4} - \frac{r_h}{r} - \ell(\ell+1) \right] \phi_1 = 0, \quad (5)$$

here  $r_h = 2M$  is the event horizon for the Schwarzschild spacetime. Such threshold, expressed in terms of the dimensionless ratio  $\alpha_t/M^2$ , depends on the multipolar distribution of the scalar perturbation  $\delta\phi$ , symbolized by the spherical harmonic index  $\ell$ , as well as the number of nodes of the scalar field  $n$ . In Table II we show the threshold for given values of  $\ell$  and  $n$ . Note that the smaller threshold  $\alpha_t$  for which scalarization occurs is for  $(\ell, n) = (0, 0)$ , and, incidentally, this leads to the faster unstable mode for  $\alpha > \alpha_t$  in some theories [24].

### III. BACKGROUND SOLUTIONS AND LINEAR ORDER PERTURBATIONS

In this work we focus on spherically symmetric BH spacetimes

$$ds^2 = -A(r)dt^2 + \frac{dr^2}{B(r)} + r^2 d\Omega^2, \quad (6)$$

where  $d\Omega^2 = d\theta^2 + \sin^2\theta d\varphi^2$  is the line element of the 2-sphere. In analytical symbolic computations, it is convenient to use  $\chi = \cos\theta$  instead of the  $\theta$  to speed up the analysis.

To compute QNMs we need to determine the numerical BH background in which the tensor and scalar perturbations propagate. The procedure was already thoroughly (see, e.g., Refs. [25, 26, 28]) explored in the literature, but we outline it here for completeness. The background field equations are given in Appendix A. We start by demanding that the metric components in Eq. (6) have the proper behavior describing a BH. Near the event horizon, this is equivalent to considering the following expansions

$$A(r) = \sum_{n=1} a^{(n)}(r-r_h)^n, \quad (7)$$

$$B(r) = \sum_{n=1} b^{(n)}(r-r_h)^n, \quad (8)$$

$$\phi_0(r) = \sum_{n=0} \phi^{(n)}(r-r_h)^n, \quad (9)$$

where the coefficients  $\{a^{(n)}, b^{(n)}, c^{(n)}\}$  are obtained by inserting the above expansion into the field equations (2)-(3), expanding close to the horizon, and solving order by order iteratively. Far from the BH, i.e.  $r \gg r_h$ , we have that

$$A(r) = 1 - \frac{2M}{r} + \sum_{n=1} \frac{\tilde{a}^{(n)}}{r^n} \quad (10)$$

$$B(r) = 1 - \frac{2M}{r} + \sum_{n=1} \frac{\tilde{b}^{(n)}}{r^n}, \quad (11)$$

$$\phi_0(r) = \frac{Q}{r} + \sum_{n=2} \frac{\tilde{\phi}^{(n)}}{r^n}, \quad (12)$$

where  $M$  and  $Q$  are the ADM mass and the scalar charge respectively. Equations (10)-(12) are consistent with the requirement that the BH solutions are asymptotically flat. Once again, the coefficients  $\{\tilde{a}^{(n)}, \tilde{b}^{(n)}, \tilde{\phi}^{(n)}\}$  can be obtained by replacing  $A(r), B(r)$  and  $\phi(r)$  into Eqs. (2)-(3) and solving order by order in  $1/r$ .

For the theory described by the Lagrangian (1), BH solutions that are regular at the horizon are possible provided that the following existence condition is satisfied:

$$\lim_{r \rightarrow r_h} \{ J^2 r^6 - 48(\partial_\phi F)^2 r^2 [9(\partial_\phi J)^2 + 2] + 2J[r^6(3(\partial_\phi J)^2 + 1) - 48(\partial_\phi F)^2 r_h^2] - 1152(\partial_\phi F)^3 \partial_\phi J + r^6[3(\partial_\phi J)^2 + 1]^2 \} \geq 0, \quad (13)$$

Note that the first derivative of the scalar field at the horizon is given in terms of the parameters  $\alpha, \beta$ , and of the value of  $\phi$  at  $r_h, \phi_h$ .

We can now introduce linear order perturbations as

$$g_{\mu\nu} = g_{\mu\nu}^{\text{BG}} + \varepsilon \delta h_{\mu\nu}, \quad \phi = \phi_0 + \varepsilon \delta\phi, \quad (14)$$

where  $\varepsilon \ll 1$  is a bookkeeping parameter representing the order of the perturbation. The quantities with superscript BG correspond to the numerical background solutions and depend only on the radial coordinate  $r$ , while the perturbations are functions of  $(t, r, \chi, \varphi)$ . The symmetry of the background allows to expand metric perturbations into tensor spherical harmonics  $T_{\mu\nu}^{\ell m}(\chi, \varphi)$ , which depend on the usual spherical harmonics  $Y_\ell^m$  and their derivatives [55, 56]. This leads  $\delta h_{\mu\nu}$  to separate into axial and polar sectors according to their properties under a parity transformation. For a spherical background such components decouple and can be treated independently

$$\delta h_{\mu\nu}(t, r, \chi, \varphi) = \sum_{\ell m} \{ [h_{\mu\nu}^{\ell m}(r, t) T_{\mu\nu}^{\ell m}(\chi, \varphi)]_{\text{ax}} + \sum_{\ell m} [h_{\mu\nu}^{\ell m}(r, t) T_{\mu\nu}^{\ell m}(\chi, \varphi)]_{\text{pol}} \}, \quad (15)$$

In the same spirit, the scalar perturbation can be decomposed in terms the spherical harmonics and reads

$$\delta\phi = \sum_{\ell m} \frac{\phi_1^{\ell m}(t, r)}{r} Y_\ell^m(\chi, \varphi). \quad (16)$$

Because of the parity properties of the scalar field perturbations the axial metric perturbations decouple from the scalar field perturbations. For the polar sector, however, metric and scalar perturbations couple with each other, similarly to what happens for EdGB BHs [44].

In this work we focus on the axial sector only. Then, adopting the Regge-Wheeler gauge, the components of the metric perturbations in Eq. (15) take the following form:

$$[h_{\mu\nu}^{\ell m} T_{\mu\nu}^{\ell m}]_{\text{ax}} = \begin{pmatrix} 0 & 0 & 0 & (\chi^2 - 1) h_0^{\ell m} \\ 0 & 0 & 0 & (\chi^2 - 1) h_1^{\ell m} \\ 0 & 0 & 0 & 0 \\ * & * & 0 & 0 \end{pmatrix} \partial_\chi Y^{\ell m}. \quad (17)$$

The field equations relevant for computing  $h_0^{\ell m}, h_1^{\ell m}$  are shown in Appendix B. For the sake of clarity, hereafter we take the sum on  $(\ell, m)$  to be implicit and we also drop the multipolar indices.

### A. Time and frequency domain integration

By expanding the field equations (2)-(3) up to first order in  $\varepsilon$ , we obtain the differential equations for the metric components  $h_0$  and  $h_1$ . We solve such equations in the time and frequency domain, resorting to different techniques.

For the time evolution it is useful to cast the equations for axial perturbations in terms of a single master equation for  $h_1$ :

$$g(r)^2 \frac{\partial^2 h_1}{\partial t^2} - \frac{\partial^2 h_1}{\partial r^2} + C(r) \frac{\partial h_1}{\partial r} + U(r) h_1 = 0, \quad (18)$$

where the coefficients  $g(r)$  and  $C(r)$  depend only on the background solution. We study the time evolution of such equation adopting a set of lightcone coordinates [57, 58]  $u = t - r_*$  and  $v = t + r_*$ , such that the Eq. (18) can be re-written as:

$$\left[ 4 \frac{\partial^2}{\partial u \partial v} + V_a(u, v) \right] Z(u, v) = 0, \quad (19)$$

where  $V_a$  reduces to the Regge-Wheeler potential in GR in the appropriate limit. As initial conditions we consider a static Gaussian pulse, *i.e.*,

$$Z(0, v) = A \exp \left[ -\frac{(v - v_0)^2}{2\sigma^2} \right], \quad Z(u, 0) = 0. \quad (20)$$

We fix the width of the Gaussian pulse to  $\sigma = 5M$  and the constant  $v_0 = 25M$ , checking that our results are independent of these choices. As the equation is linear, we can freely scale the amplitude to  $A = 1$ . The time domain profile of the signal is extracted at  $r = 25M$ , setting the integration domain to  $(u, v) \in [0, 400M]$ , which is large enough to capture the QNM ringing. Frequencies and damping times of a given mode are then computed

by numerically fitting the signal with damped sinusoids. We have carefully chosen the ringdown time extraction to avoid any initial data-dependent signal or late-time tail behavior, verifying that the frequency response and damping time is numerically stable by a slight change in the ringdown time window.

When solving for the perturbations in the frequency domain we first decompose time dependent quantities in Fourier modes, such that

$$h_1(t, \omega) = \int_{-\infty}^{\infty} h_1(\omega, r) e^{-i\omega t} d\omega. \quad (21)$$

The equations for  $h_1$  and  $h_0$  can then be written in a matrix compact form as:

$$\frac{d}{dr} \Psi_i + C_{ij} \Psi_j = 0, \quad (22)$$

where  $\Psi = (h_0, h_1)^\top$  and the coefficients  $C_{ij}$  depend on the numerical background and on  $\omega$ . We solve Eqs. (22) through the so called matrix method [59]. We first impose suitable boundary conditions which identify purely ingoing waves at the horizon and purely outgoing waves at infinity:

$$\Psi_i^a(r_* \rightarrow -\infty) = \sum_{n_{\min}}^{n_{\max}} c_i^{(n)} e^{-i\omega r_*} (r - r_h)^n \quad (23)$$

$$\Psi_i^a(r_* \rightarrow +\infty) = \sum_{n_{\min}}^{n_{\max}} \frac{\bar{c}_i^{(n)}}{r^n} e^{i\omega r_*}, \quad (24)$$

where the coefficients  $(c_i^{(n)}, \bar{c}_i^{(n)})$  can be found with the same iterative procedure adopted for Eqs. (7)-(9), and are all proportional to the leading term of one of the two metric perturbations.

Let us first examine the behavior of the boundary conditions of the perturbations. At the horizon, the leading order coefficients in (23) are given by

$$h_0 = c_1^{(0)} + \mathcal{O}(r - r_h), \quad (25)$$

$$h_1 = \frac{c_1^{(0)}}{\sqrt{a^{(1)} b^{(1)}} (r - r_h)} + \mathcal{O}(1), \quad (26)$$

where  $c_1^{(0)}$  is the leading order amplitude for  $h_0$ , and serves as a free parameter. The expressions written above coincide with those obtained in GR. Deviations enter therefore at the next to leading order in the expansion, specifically as:

$$\frac{h_0^{(1)}}{h_0^{(0)}} = \frac{N_0}{D_0}, \quad \frac{h_1^{(1)}}{h_0^{(0)}} = \frac{N_1}{D_1}, \quad (27)$$

where

$$N_{0,1} = f_{\ell, \omega}(a^{(1)}, b^{(1)}, \phi^{(1)}, a^{(2)}, b^{(2)}, \phi^{(2)}, J|_0, \partial_\phi J|_0) \partial_\phi F|_0, \partial_\phi^2 F|_0 \quad (28)$$

$$D_{0,1} = f_\omega(a^{(1)}, b^{(1)}, \phi^{(1)}, J|_0, \partial_\phi F|_0) \quad (29)$$

where in this context  $f_\omega, f_{\ell,\omega}$  denote arbitrary functions depending on  $\omega$  and  $(\ell, \omega)$  respectively.

We fix<sup>1</sup>  $n_{\max} = 4$  for the horizon perturbations and  $n_{\max} = 7$  at asymptotic infinity. Then, we create the  $2 \times 2$  fundamental matrix given by two independent solutions of Eq. (22):

$$\mathbf{X}_a = (\Psi_{(h)}^a, \Psi_{(\infty)}^a) = \begin{pmatrix} h_0^{(h)} & h_0^{(\infty)} \\ h_1^{(h)} & h_1^{(\infty)} \end{pmatrix}. \quad (30)$$

The first solution ( $h$ ) is obtained by integrating the differential equations (22) from the horizon outward with boundary condition (23), while the second ( $\infty$ ) is determined by integrating from infinity inward using as boundary conditions Eqs. (24). QNM frequencies correspond to poles of the determinant of the fundamental matrix, *i.e.* they are given by solving

$$\det \mathbf{X}(\omega)|_{r_m} = 0, \quad (31)$$

while we check that our results are independent of the choice for the intermediate matching point radius  $r_m$ .

## B. The scattering potential

Equation (18) allows a straightforward check for the stability of the solutions [33, 60–62]. To this aim, we first transform  $h_1$  in the frequency domain, introduce then a generalised tortoise coordinate

$$\frac{dr_*}{dr} = g(r) = \sqrt{\frac{1 + J - 2(\partial_\phi F)B'\phi' - 4B[\phi'(\partial_\phi F)]'}{B[A(J+1) - 2B(\partial_\phi F)A'\phi']}}, \quad (32)$$

and replace  $h_1 \rightarrow f(r)Z$ , where  $f(r)$  is a generic function of the radial coordinate. We can then choose  $f(r)$  such that Eq. (18) is cast into a Regge-Wheeler type form, *i.e.*

$$\left[ \frac{d^2}{dr_*^2} + \omega^2 \right] Z = V_a Z, \quad (33)$$

To assess the stability of the solution we then integrate (33) as

$$\int dr_* \omega^2 |Z|^2 = \int dr_* \left[ \left| \frac{dZ}{dr_*} \right|^2 + V_a |Z|^2 \right] - Z^* \frac{dZ}{dr_*} \Big|_{-\infty}^{+\infty}, \quad (34)$$

where  $\Phi^*$  is the complex conjugate of the perturbation. The last term on the right hand side of Eq. (34) vanishes, since for unstable modes  $Z = 0$  both at the horizon and

at infinity. Then, a sufficient condition for the presence of unstable solutions is given by

$$\int_{-\infty}^{+\infty} dr_* V_a < 0. \quad (35)$$

We can now introduce an arbitrary function  $S$ , that does not diverge at the boundaries, such as to re-write Eq. (34) as

$$\int dr_* \omega^2 |Z|^2 = \int dr_* \left[ \left| \frac{dZ}{dr_*} + ZS \right|^2 + \hat{V}_a |Z|^2 \right], \quad (36)$$

where  $\hat{V}_a = V_a + dS/dr_* - S^2$  is the  $S$ -deformed potential. If the latter is non-negative everywhere, then modes are stable. The existence  $S$ , and hence the stability of the solution, can be checked by solving the equation [60]:

$$V_a + \frac{dS}{dr_*} - S^2 = 0. \quad (37)$$

Before closing this subsection let us refer to the issue regarding the hyperbolicity of Eq. (18). When dealing with the numerical evolution of a given set of initial data, we need to be particularly cautious about the hyperbolic character of the partial differential equations that describe the evolution (see for example [63] for a discussion on the problem of well-posedness in GR). In our case, examining the hyperbolic nature of Eq. (18) is fairly straightforward as it is determined by the sign of  $g(r)$ , which then depends on the specific model considered. Previous calculations showed that, for theories that do not feature the scalar-Ricci coupling, hyperbolicity may be lost in certain regions of the parameter space [24]. However, It was later shown in [28] that including the Ricci coupling can render the evolution equations hyperbolic at perturbative level. Ref. [42] considered spherical collapse and found that this coupling has the same effect at nonlinear level.

## IV. NUMERICAL RESULTS

### A. A case study

To investigate the QNM properties for charged BHs we first consider a specific case study, focusing on Es-  
RGB gravity with  $\beta = 10$ . Black holes in this theory are radially stable, and their charge can be taken to be large enough to significantly affect the background geometry. The charge  $Q/M$  of such solutions as a function of the coupling  $\alpha/M^2$  is shown in Fig. 1.

We focus on four representative cases in the parameter space, with the corresponding axial potentials drawn in Fig. 2. The first one, just at the onset of the scarization and represented by the label  $\odot$ , corresponds to a Schwarzschild BH in GR and works as a comparison model for the scalarized BHs. The  $\Delta$  marker represents a configuration with an intermediate value of  $Q/M$ , and

<sup>1</sup> We have checked that higher order expansions do not improve our numerical calculations.

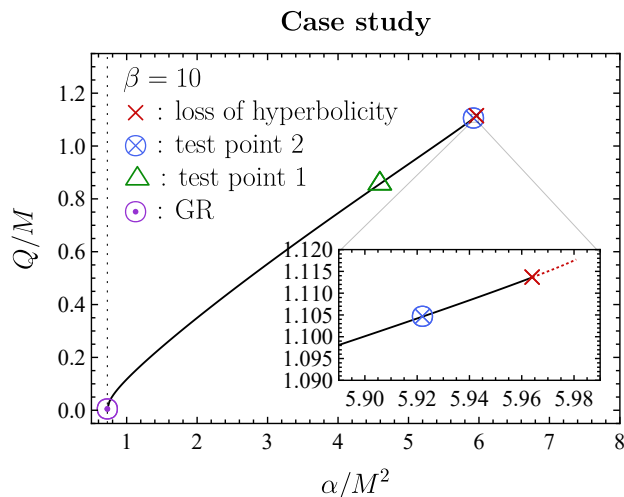


FIG. 1. Black hole charge as a function of  $\alpha/M^2$  in EsRGB gravity assuming  $\beta = 10$ . Colored markers identify four specific configurations given by the GR limit, a solution close to the parameter space in which the hyperbolicity of Eq. (18) is lost, and two test cases with large values of the charge. Configurations for which hyperbolicity breaks are drawn with a dashed line in the zoomed inset plot.

features a scattering potential similar to the GR case. Finally, we consider two highly charged solutions, identified by  $\otimes$  and  $\times$ , with the latter being close to the onset of the hyperbolicity loss (see the inset of Fig. 1). For the  $\otimes$  and  $\times$  solutions the axial potential becomes negative for some values of  $r_* < 0$  (see Fig. 2), affecting the late-time behavior of the perturbations.

Before computing the actual values of the QNMs, we analyze the  $S$ -deformed potential to investigate whether our configurations are stable. In all cases studied it is possible to find the  $S$ -deformed potential, such that Eq. (37) is satisfied. As an example, in the right panel of Fig. 1 we plot the scattering and the corresponding  $S$ -deformed potential for the  $\triangle$  and the  $\otimes$  test points.

We can now move to study the dependence of the QNM frequencies on the BH charge. In Fig. 3 we plot the real and the imaginary part of the  $\ell = 2$  fundamental mode as a function of  $\alpha/M^2$ . All values are normalised to the corresponding GR limit, i.e.  $\omega_{\ell=2}^{\text{GR}} \approx 0.3737 - i 0.08896$ . The real component of  $\omega$  tends to increase for larger couplings, varying by less than  $\sim 8\%$  as  $\alpha/M^2$  approaches the value at which hyperbolicity is broken<sup>2</sup>. The imaginary part however changes considerably and decreases monotonically, varying by up to 80% compared to  $\omega_i^{\text{GR}}$ . This indicates that axial modes for scalarized solutions in EsRGB gravity can live considerably longer than those of Schwarzschild BHs.

Such results are confirmed by a time-evolution study

of the perturbations, shown in Fig. 4 for the four BH configurations we focused on, and  $\ell = 2$ . After an initial growth, which depends on the initial data, we observe the signal setting into the usual, exponentially damped, oscillatory behavior. Differences between the four models are mainly controlled by changes in the scattering potential. As expected, perturbations for the  $\otimes$  and  $\times$  models show a slower decay. We have numerically extracted the values of the frequency and of the damping time for each perturbation, finding good agreement with the results obtained with the frequency domain analysis.

## B. Potential and quasinormal modes

Having used the special case  $\beta = 10$  in the EsRGB scenario as a demonstration of how our analysis proceeds, we now broaden the discussion to the axial potential and QNMs concerning the EdRGB, EsRGB, and EsGB theories as those were introduced in Sec. II.

In the three panels included in Fig. 5 we plot the axial potential for angular number  $\ell = 2$  in the three different theories. As has already been explained, after fixing the parameters  $\beta, \zeta$ , there is a range of values for the GB coupling  $\alpha$  that allows for asymptotically flat black holes with a vanishing scalar field, which explains the different values of  $\alpha$  explored in each theory subset in Fig. 5. In principle, the larger  $\alpha/M^2$  is, the more the black hole deviates from GR. For EdRGB and EsRGB, we plot the potential for  $\beta = 0$  and  $\beta = 5$ . For EsGB we only plot the potential for  $\zeta/\alpha = -1$ , since in the limit  $\zeta/\alpha \rightarrow 0$  the theory coincides with EsRGB for  $\beta \rightarrow 0$ .

We see that when  $\beta = 0$  in EsRGB and EsGB, or  $\zeta/\alpha = 0$  in EsGB, the potential remains positive and relatively unchanged along the allowed range for  $\alpha/M^2$ . Introducing the additional couplings ( $\beta, \zeta$ ) significantly affects the form of the potential. In particular, in EdRGB and EsRGB the potential develops an increasingly negative region when one moves along the  $\alpha/M^2$  “existence lines”. In the EsGB case for a negative ratio  $\zeta/\alpha$ , and as one moves along the existence line towards larger values for  $\alpha/M^2$ , the potential develops local minima in addition to the one corresponding to the negative region.

We then move on to calculating the QNM frequencies according to the integration method we described in Sec. III. In Fig. 6, we present the results in the EdRGB scenario. For  $\beta = 0$  and  $\ell = 2$ , the results are in agreement with those recovered in [44]. Increasing the values of  $\beta$ , results in increasingly larger deviations from GR particularly towards the end of the existence line, where the ratio  $\alpha/M^2$  is maximized. In accordance to the form of the effective potential for large  $\alpha/M^2$ , which showed the appearance of a negative region, the ratio of the imaginary part of the QNM frequencies tends to smaller positive values, but never reaches zero. It is worth pointing out that according to the  $S$ -deformed potential method, no unstable modes are found, consistently with the aforementioned results. It is also worth-noting that for  $\ell = 2$ ,

<sup>2</sup> Note that when hyperbolicity is lost, modes can still be numerically computed

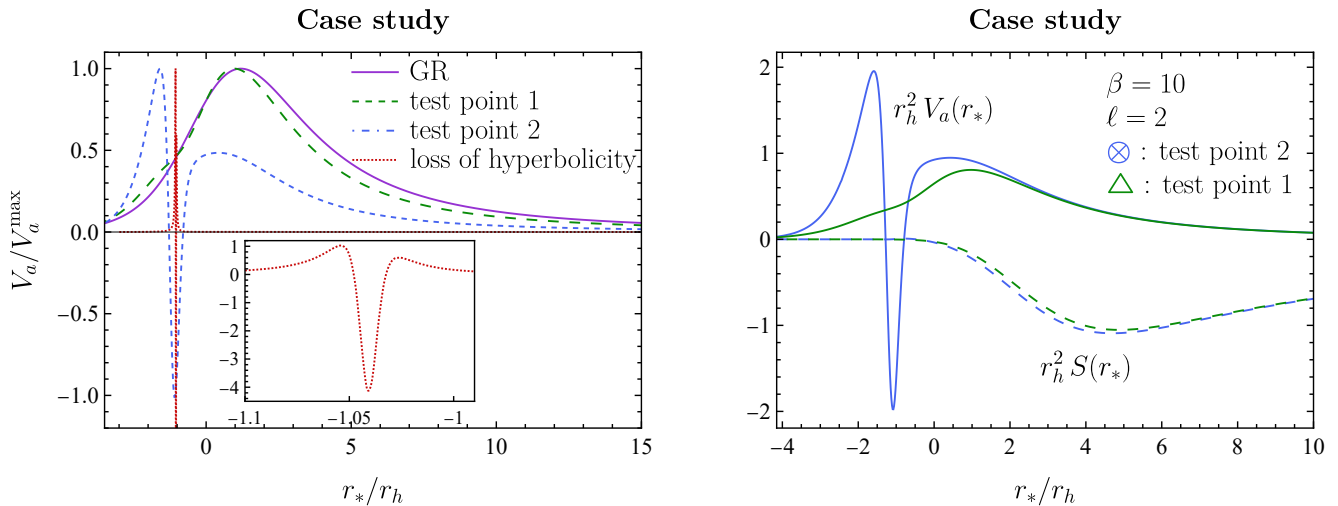


FIG. 2. *Left*: Axial  $\ell = 2$  scattering potential for the four BH configurations shown in Fig. 1, normalized by its maximum value. The inset focuses on the critical range where hyperbolicity is lost for the  $\times$  model. *Right*: Comparison between the  $\ell = 2$  axial (solid curves) and S-deformed (dashed curves) potentials, for the test points 1 and 2.

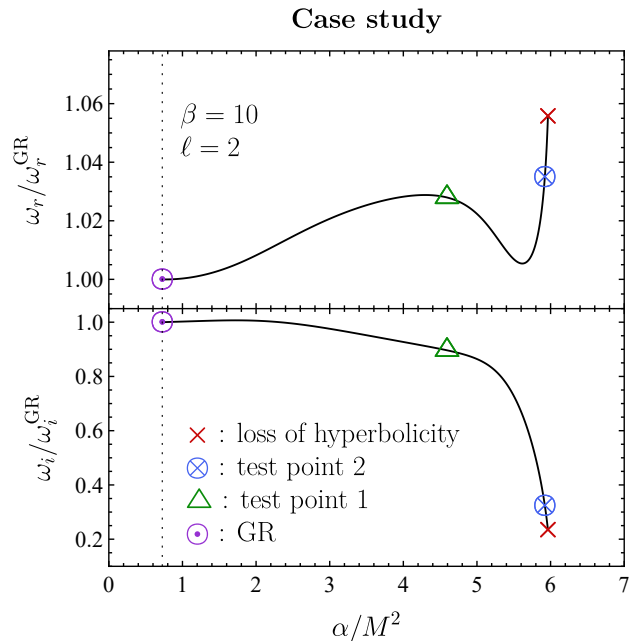


FIG. 3. Real and imaginary part of the  $\ell = 2$  mode for BHs in EsRGB gravity with  $\beta = 10$ , as a function of the coupling  $\alpha/M^2$ . All frequencies are normalised to the Schwarzschild values. On each curve we highlight QNM values for the four specific configurations discussed in Sec. IV A.

while both the real and imaginary parts increase towards the end of the existence line for smaller values of  $\beta$ , for larger  $\beta$  the opposite behaviour is observed. Especially the imaginary component for  $\beta = 2$  drops by as much as  $\sim 60\%$  near the edge. The real part, even though deviates significantly more than what it does in the  $\beta = 0$  scenario, it remains within around  $\sim 10\%$  of its GR counter-

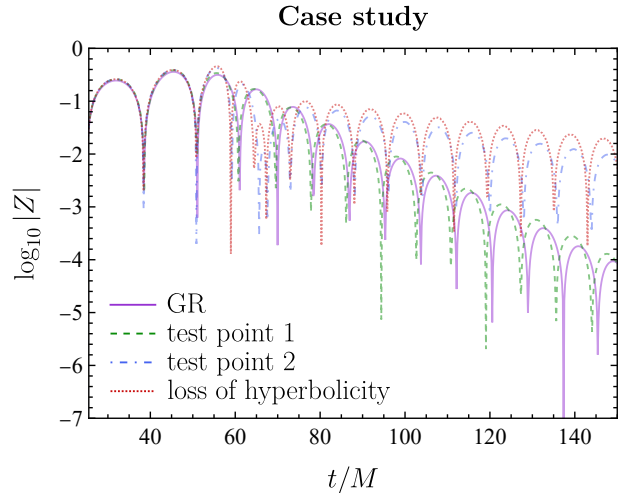


FIG. 4. Time evolution of the axial perturbation defined in Eq. (18). Different curves refer to the four BH configurations shown in FIG. 1 as colored markers. Perturbations are extracted at  $r_* = 25M$ .

part in the  $\beta = 2$  case. For  $\ell = 3$ , on the other hand, the behaviour of the QNM curves is different, *e.g.* the imaginary part for  $\beta = 1, 2$  is significantly non-monotonic along the existence lines.

Similar-scale results are depicted in Fig. 7 concerning the EsRGB model, where the vertical dashed line corresponds to the  $n = 0$  scalarization threshold. Of particular interest in this model is the  $\beta = 2$  case for which significant deviations from GR are noticed relatively close to the scalarization threshold, as is evident especially for the real part of the  $\ell = 3$  mode. Once again, in agreement with the potential presented in the middle panel of Fig. 5, the imaginary part of the QNM frequency for

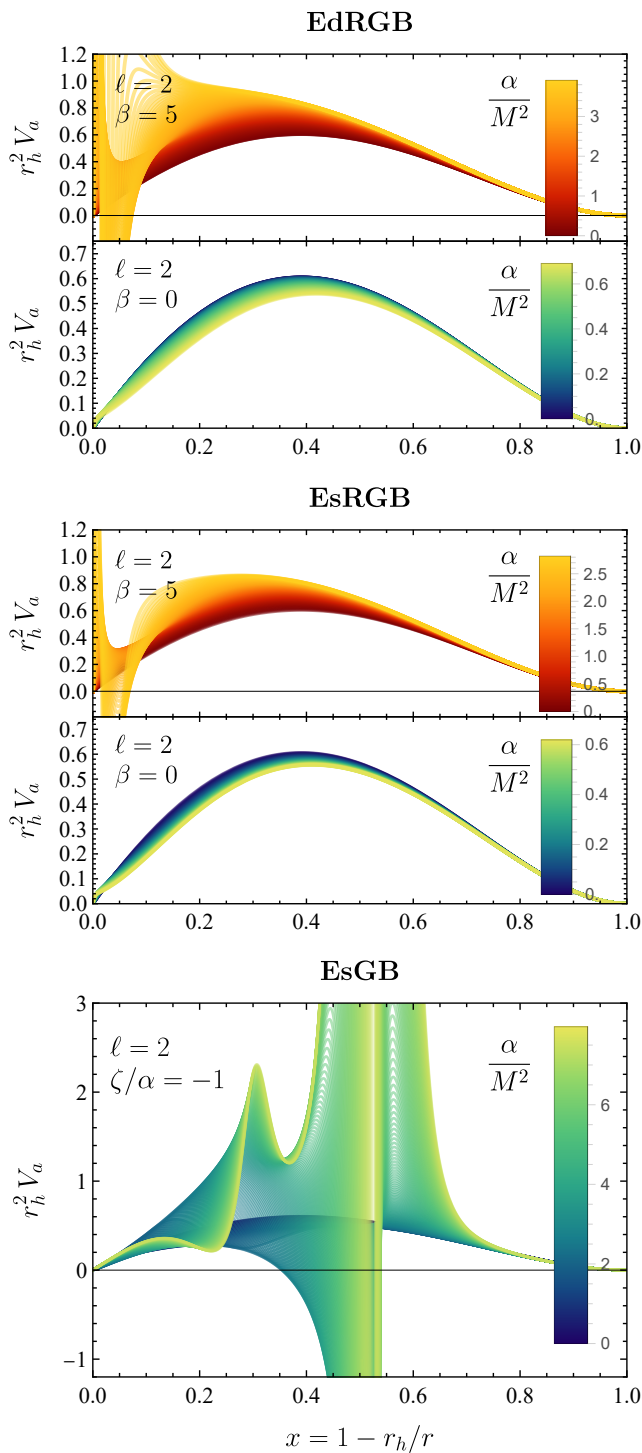


FIG. 5. *Top*: Axial potential in the EdRGB model for  $\ell = 2$  and  $\beta = 0, 2$ . Each color in the bar legend corresponds to a different potential curve created for a different value of the dimensionless coupling  $\alpha/M^2$ , spanning all the allowed values. *Middle*: Same but for the EsGB model. Here the nonzero value for the Ricci-scalar coupling is chosen to be  $\beta = 5$ . *Bottom*: Similar plot but for the EsGB model when  $\zeta/\alpha = -1, -3/2$ .

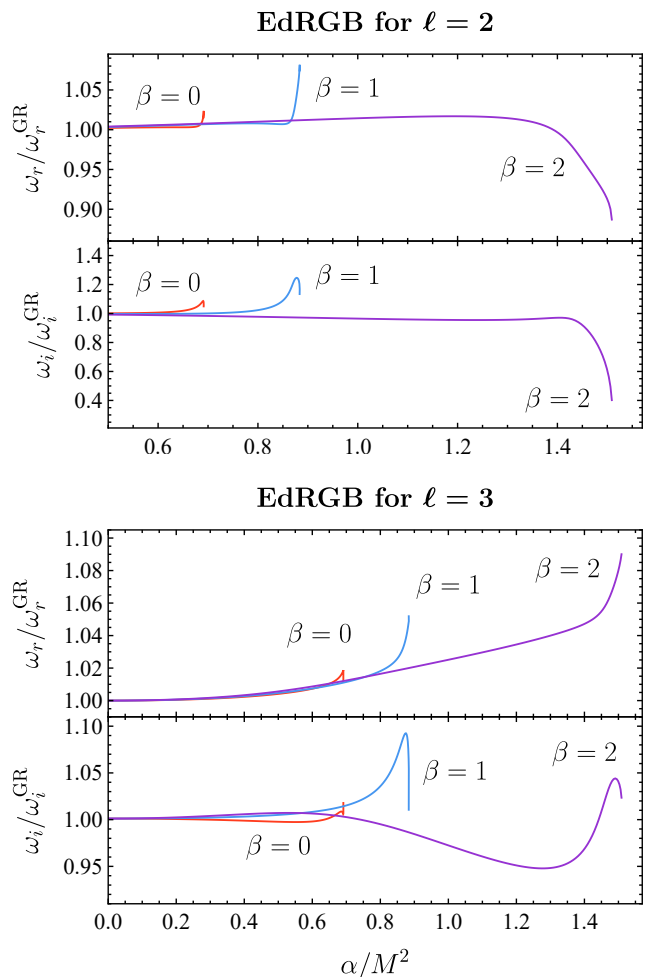


FIG. 6. *Top*: Relative ratio of the hairy black hole mode with respect to the GR one, in the EdRGB model for  $\ell = 2$  and  $\beta = 0, 1, 2$ . *Bottom*: Same as top panel but for  $\ell = 3$ .

$\ell = 2$ , becomes all the less negative, as one moves along the existence lines, but never reaches the horizontal axis.

For the EsGB case, the results are shown in Fig. 8, and between the three models, they are the ones that deviate from GR the most. It is worth emphasizing that in this model significant deviations from GR appear fairly close to the scalarization threshold regardless of the value of the ratio  $\zeta/\alpha$ .

## V. CONCLUSIONS

We have studied axial quasinormal modes of black holes with scalar hair in several models that evade no-hair theorems and, in some cases, exhibit spontaneous scalarization. We analysed perturbations in both the time and the frequency domain, extending previous studies in the literature.

In particular, we have shown that in the minimal case where the scalar couples only to the Gauss-Bonnet in-

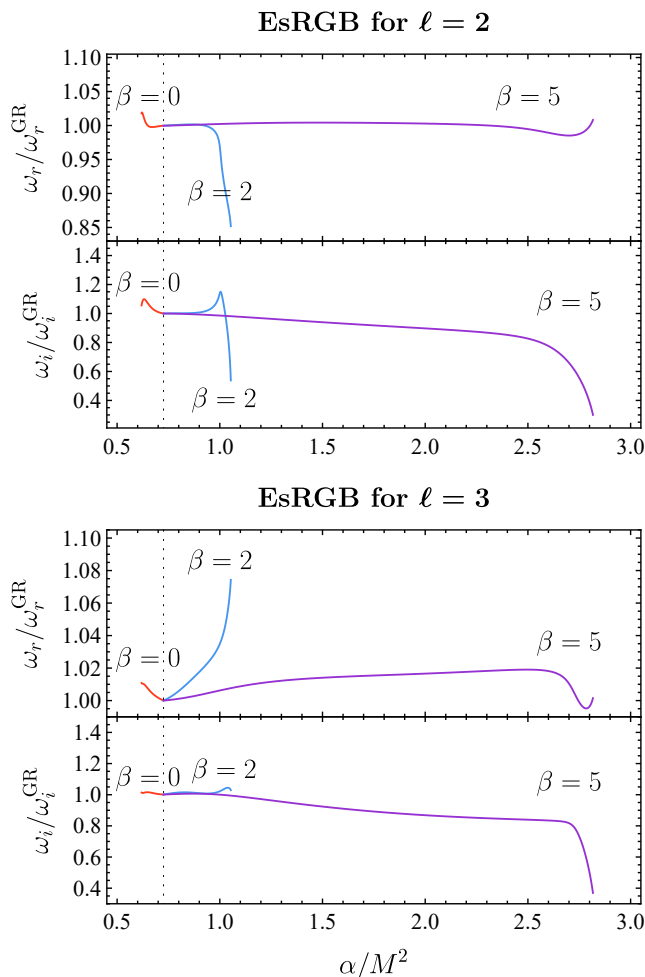


FIG. 7. *Top*: Relative ratio of the hairy black hole mode with respect to the GR one, in the EsRGB model for  $\ell = 2$  and  $\beta = 0, 2, 5$ . *Bottom*: Same as top panel but for  $\ell = 3$ .

variant, the scalar charge has a small impact on the axial perturbations, deviating only slightly from the Schwarzschild BH in GR. However, when a coupling to the Ricci scalar is added some configurations can vibrate for a significantly longer time, even though the oscillation frequency is just a few percent off from its GR counterpart.

It is worth pointing out the following. First, for the EdRGB and EsRGB theories the maximum deviation of the modes from the GR case is for smaller masses and close to the threshold mass beyond which black holes cease to exist for a given value of the coupling. This is not necessarily the case for the quadratic EsGB model. Second, the maximum deviations from GR appear in the parameter space region where the background solutions' scalar charge is also maximum. This is expected, as the charge is usually related to the intensity of the additional terms appearing in the perturbed equations.

Our analysis showed that the effective potential of axial perturbations can become negative close to the BH

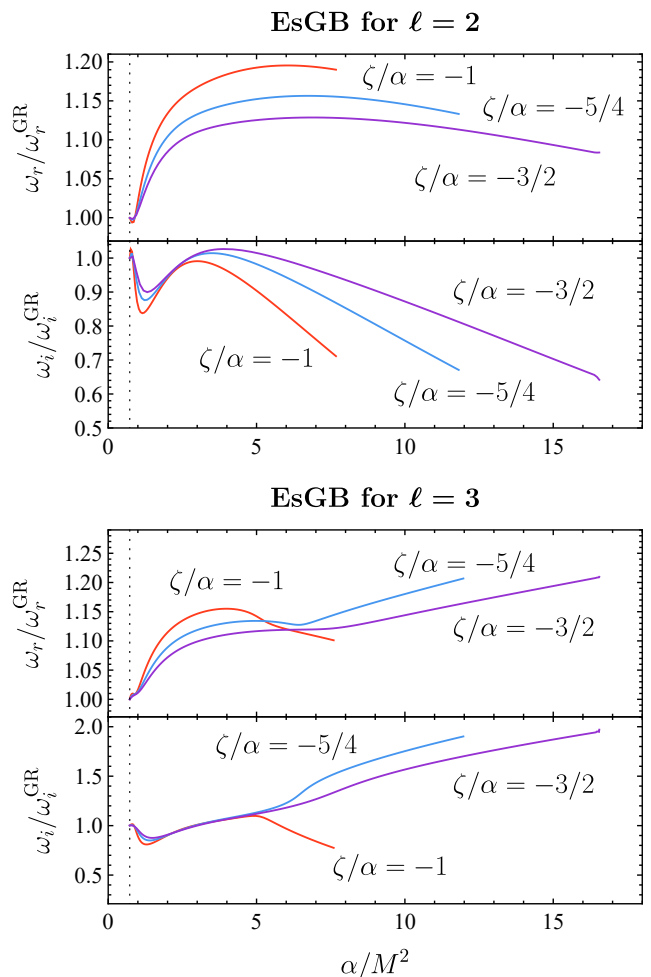


FIG. 8. *Top*: Relative ratio of the hairy black hole mode with respect to the GR one, in the EsGB model for  $\ell = 2$  and  $\zeta/\alpha = -1, -5/4, -3/2$ . *Bottom*: Same as top panel but for  $\ell = 3$ .

as we increase the coupling parameter of the additional interactions and also develop a well and an additional minimum. The potential well could indicate the existence of trapped unstable modes. However, studying the deformed potential, performing a direct integration mode computation, and performing a time-domain evolution of initial signals, we found no evidence of a mode instability. Moreover, we have also not found any discontinuous behavior of the fundamental mode and only moderate changes in the QNM frequencies. This suggests that the axial spectra of the BHs studied here are stable. This is to be contrasted with scenarios where small (ad hoc) deviations in the potential might lead to a spectral instability of the modes [64].

Our analysis is restricted to the axial sector. The polar sector is more evolved as gravitational and scalar perturbations are coupled to each other, with the scalar sector leaving a possible imprint in the ringdown. Usually, the polar sector dominates over the axial one, but in the pos-

sibility of the imaginary part of the axial modes being smaller than the polar in generalized scalar-tensor theories, this hierarchy could be broken. The axial modes could live longer than the polar ones. However, only a full computation of the spectrum would reveal the hierarchy, which is a natural extension of this work.

The lifetimes of axial and polar modes play a crucial role on the detectability of GR deviations which, for theories of gravity with dimensionful couplings, represent a difficult challenge. A recent analysis for EdGB dilatonic BHs suggested that, even with next generation detectors, ringdown observations alone may not be sufficient to measure the coupling of the theory [65], since constraints are dominated by light objects with low signal to noise ratios. Our results, however, show that deviations in the QNM spectrum increase for scalarized BHs, leading in particular to modes with significant longer damping times. We plan to assess the ability of 3g interferometers to detect such changes having computed the full axial and polar sector.

### ACKNOWLEDGMENTS

C.F.B.M. would like to thank Fundação Amazônia de Amparo a Estudos e Pesquisas (FAPESPA), Conselho Nacional de Desenvolvimento Científico e Tecnológico (CNPq) and Coordenação de Aperfeiçoamento de Pessoal de Nível Superior (CAPES) – Finance Code 001, from Brazil, for partial financial support. A. M. acknowledges partial support from MUR PRIN Grant No. 2022-Z9X4XS, funded by the European Union - Next Generation EU. T.P.S. acknowledges partial support from the STFC Consolidated Grants no. ST/X000672/1 and no. ST/V005596/1.

### Appendix A: Background equations

Here we provide the explicit form of the background equations (2) and (3) in the metric ansatz (6). From the nontrivial components of the Einstein field equations at zeroth order and the background equation of motion for the scalar field we find

$$(tt) : \quad 4 + 2r^2V - 8\partial_\phi FB' \phi' + 16B^2(\partial_\phi F \phi'' + \partial_\phi^2 F (\phi')^2) - B(-24\partial_\phi FB' \phi' + 4J + 4r^2\partial_\phi J \phi'' + 4r^2\partial_\phi^2 J (\phi')^2 + r^2(\phi')^2 + 8r\partial_\phi J \phi' + 16\partial_\phi F \phi'' + 16\partial_\phi^2 F (\phi')^2 + 4) - 4J(rB' - 1) - 2r^2\partial_\phi JB' \phi' - 4rB' = 0, \quad (A1)$$

$$(rr) : \quad 4J + -2BA'(4(3B - 1)\partial_\phi F \phi' - 2Jr - r(r\partial_\phi J \phi' + 2)) - A(B(-4J + r^2(\phi')^2 - 8r\partial_\phi J \phi' - 4) + 2r^2V + 4) = 0, \quad (A2)$$

$$(\phi) : \quad A(A(r^2(B' \phi' + 2V'(\phi)) + \partial_\phi J(4 - 4rB')) - A'B'(r^2\partial_\phi J + 4\partial_\phi F)) - 4B^2\partial_\phi F((A')^2 - 2AA'') + B(-2A(A''(r^2\partial_\phi J + 4\partial_\phi F) + A(2\partial_\phi J - r(r\phi'' + 2\phi'))) + AA'(12\partial_\phi FB' + r(r\phi' - 4\partial_\phi J)) + (A')^2(r^2\partial_\phi J + 4\partial_\phi F)) = 0. \quad (A3)$$

### Appendix B: Perturbation equations

In this appendix we provide the explicit form of the ODEs for the axial perturbations  $(h_0(r), h_1(r))$  in Eq. (17):

$$(r\chi) : \quad h'_0 - \frac{2h_0}{r} + ih_1\{A^2[2J(rB' + \ell^2 + \ell - 2) + 2r^2(\partial_\phi J)B' \phi' + 2rB' + 4Br^2(\partial_\phi J)\phi'' + 4Br^2(\partial_\phi^2 J)\phi'^2 + Br^2\phi'^2 + 4Br(\partial_\phi J)\phi' - 2r^2V(\phi) + 2\ell^2 + 2\ell - 4] + BrA'^2(4B(\partial_\phi F)\phi' - Jr - r) - 8B^2r((\partial_\phi^2 F)A'\phi'^2 + A[r^2(A'B' - 2\omega^2) + (\partial_\phi F)(A''\phi' + A'\phi'')]) + Jr(rA'B' + 2B(rA'' + A') - 2r\omega^2) + 2B(r(rA'' + 4(\partial_\phi F)\omega^2\phi') + A'(r(r(\partial_\phi J)\phi' + 1) - 2(\partial_\phi F)\phi'(3rB' + \ell^2 + \ell - 2)))]\} / 2Ar\omega(-Jr + 4B(\partial_\phi F)\phi' - r) = 0, \quad (B1)$$

$$(\theta\chi) : \quad h'_1 - h_0, i\omega[2(\partial_\phi F)B' \phi' + 4B(\partial_\phi F)\phi'' + 4B(\partial_\phi^2 F)\phi'^2 - J - 1] / \{B[A(J + 1) - 2B(\partial_\phi F)A'\phi']\} + h_1\{[A^2((J + 1)B' + 2B(\partial_\phi J)\phi')] + 2B^2(\partial_\phi F)A'^2\phi'\} \quad (B2)$$

$$- AB[4B(\partial_\phi F)A''\phi' + A'(6(\partial_\phi F)B'\phi' + 4B(\partial_\phi F)\phi'' + 4B(\partial_\phi^2 F)\phi'^2 - J - 1)]\} / [2ABA(J + 1) - 2B(\partial_\phi F)A'\phi'] = 0.$$

- 
- [1] B. P. Abbott *et al.* (LIGO Scientific, Virgo), *Phys. Rev. Lett.* **116**, 061102 (2016), arXiv:1602.03837 [gr-qc].
- [2] B. P. Abbott *et al.* (LIGO Scientific, Virgo), *Phys. Rev. X* **9**, 031040 (2019), arXiv:1811.12907 [astro-ph.HE].
- [3] R. Abbott *et al.* (LIGO Scientific, Virgo), *Phys. Rev. X* **11**, 021053 (2021), arXiv:2010.14527 [gr-qc].
- [4] R. Abbott *et al.* (LIGO Scientific, VIRGO), (2021), arXiv:2108.01045 [gr-qc].
- [5] R. Abbott *et al.* (LIGO Scientific, VIRGO, KAGRA), (2021), arXiv:2111.03606 [gr-qc].
- [6] G. W. Horndeski, *Int. J. Theor. Phys.* **10**, 363 (1974).
- [7] C. Deffayet, S. Deser, and G. Esposito-Farese, *Phys. Rev. D* **80**, 064015 (2009), arXiv:0906.1967 [gr-qc].
- [8] T. Kobayashi, M. Yamaguchi, and J. Yokoyama, *Prog. Theor. Phys.* **126**, 511 (2011), arXiv:1105.5723 [hep-th].
- [9] B. Elder and J. Sakstein, *Phys. Rev. D* **107**, 044006 (2023), arXiv:2210.10955 [gr-qc].
- [10] J. D. Bekenstein, *Phys. Rev. D* **51**, R6608 (1995).
- [11] S. W. Hawking, *Commun. Math. Phys.* **25**, 167 (1972).
- [12] T. P. Sotiriou and V. Faraoni, *Phys. Rev. Lett.* **108**, 081103 (2012), arXiv:1109.6324 [gr-qc].
- [13] H. O. Silva, J. Sakstein, L. Gualtieri, T. P. Sotiriou, and E. Berti, *Phys. Rev. Lett.* **120**, 131104 (2018), arXiv:1711.02080 [gr-qc].
- [14] S. Mignemi and N. R. Stewart, *Phys. Lett. B* **298**, 299 (1993), arXiv:hep-th/9206018.
- [15] P. Kanti, N. E. Mavromatos, J. Rizos, K. Tamvakis, and E. Winstanley, *Phys. Rev. D* **54**, 5049 (1996), arXiv:hep-th/9511071.
- [16] T. P. Sotiriou and S.-Y. Zhou, *Phys. Rev. Lett.* **112**, 251102 (2014), arXiv:1312.3622 [gr-qc].
- [17] G. Antoniou, A. Bakopoulos, and P. Kanti, *Phys. Rev. Lett.* **120**, 131102 (2018), arXiv:1711.03390 [hep-th].
- [18] D. D. Doneva and S. S. Yazadjiev, *Phys. Rev. Lett.* **120**, 131103 (2018), arXiv:1711.01187 [gr-qc].
- [19] T. P. Sotiriou and S.-Y. Zhou, *Phys. Rev. D* **90**, 124063 (2014), arXiv:1408.1698 [gr-qc].
- [20] N. Yunes and L. C. Stein, *Phys. Rev. D* **83**, 104002 (2011), arXiv:1101.2921 [gr-qc].
- [21] A. Maselli, P. Pani, L. Gualtieri, and V. Ferrari, *Phys. Rev. D* **92**, 083014 (2015), arXiv:1507.00680 [gr-qc].
- [22] A. Dima, E. Barausse, N. Franchini, and T. P. Sotiriou, *Phys. Rev. Lett.* **125**, 231101 (2020), arXiv:2006.03095 [gr-qc].
- [23] N. Andreou, N. Franchini, G. Ventagli, and T. P. Sotiriou, *Phys. Rev. D* **99**, 124022 (2019), [Erratum: *Phys.Rev.D* 101, 109903 (2020)], arXiv:1904.06365 [gr-qc].
- [24] J. L. Blázquez-Salcedo, D. D. Doneva, J. Kunz, and S. S. Yazadjiev, *Phys. Rev. D* **98**, 084011 (2018), arXiv:1805.05755 [gr-qc].
- [25] H. O. Silva, C. F. B. Macedo, T. P. Sotiriou, L. Gualtieri, J. Sakstein, and E. Berti, *Phys. Rev. D* **99**, 064011 (2019), arXiv:1812.05590 [gr-qc].
- [26] C. F. B. Macedo, J. Sakstein, E. Berti, L. Gualtieri, H. O. Silva, and T. P. Sotiriou, *Phys. Rev. D* **99**, 104041 (2019), arXiv:1903.06784 [gr-qc].
- [27] G. Antoniou, A. Lehébel, G. Ventagli, and T. P. Sotiriou, *Phys. Rev. D* **104**, 044002 (2021), arXiv:2105.04479 [gr-qc].
- [28] G. Antoniou, C. F. B. Macedo, R. McManus, and T. P. Sotiriou, *Phys. Rev. D* **106**, 024029 (2022), arXiv:2204.01684 [gr-qc].
- [29] D. Ayzenberg and N. Yunes, *Phys. Rev. D* **90**, 044066 (2014), [Erratum: *Phys.Rev.D* 91, 069905 (2015)], arXiv:1405.2133 [gr-qc].
- [30] C. A. R. Herdeiro, E. Radu, H. O. Silva, T. P. Sotiriou, and N. Yunes, *Phys. Rev. Lett.* **126**, 011103 (2021), arXiv:2009.03904 [gr-qc].
- [31] P. Kanti, N. E. Mavromatos, J. Rizos, K. Tamvakis, and E. Winstanley, *Phys. Rev. D* **57**, 6255 (1998), arXiv:hep-th/9703192.
- [32] C. F. B. Macedo, *Int. J. Mod. Phys. D* **29**, 2041006 (2020), arXiv:2002.12719 [gr-qc].
- [33] J. L. Blázquez-Salcedo, D. D. Doneva, S. Kahlen, J. Kunz, P. Nedkova, and S. S. Yazadjiev, *Phys. Rev. D* **101**, 104006 (2020), arXiv:2003.02862 [gr-qc].
- [34] M. Minamitsuji, S. Mukohyama, and S. Tsujikawa, (2024), arXiv:2403.10048 [gr-qc].
- [35] L. K. Wong, C. A. R. Herdeiro, and E. Radu, *Phys. Rev. D* **106**, 024008 (2022), arXiv:2204.09038 [gr-qc].
- [36] J. L. Ripley and F. Pretorius, *Phys. Rev. D* **101**, 044015 (2020), arXiv:1911.11027 [gr-qc].
- [37] W. E. East and J. L. Ripley, *Phys. Rev. D* **103**, 044040 (2021), arXiv:2011.03547 [gr-qc].
- [38] W. E. East and J. L. Ripley, *Phys. Rev. Lett.* **127**, 101102 (2021), arXiv:2105.08571 [gr-qc].
- [39] D. D. Doneva, F. M. Ramazanoğlu, H. O. Silva, T. P. Sotiriou, and S. S. Yazadjiev, *Rev. Mod. Phys.* **96**, 015004 (2024), arXiv:2211.01766 [gr-qc].
- [40] G. Ventagli, G. Antoniou, A. Lehébel, and T. P. Sotiriou, *Phys. Rev. D* **104**, 124078 (2021), arXiv:2111.03644 [gr-qc].
- [41] G. Antoniou, L. Bordin, and T. P. Sotiriou, *Phys. Rev. D* **103**, 024012 (2021), arXiv:2004.14985 [gr-qc].
- [42] F. Thaalba, M. Bezares, N. Franchini, and T. P. Sotiriou, (2023), arXiv:2306.01695 [gr-qc].
- [43] J. L. Blázquez-Salcedo, F. S. Khoo, and J. Kunz, *Phys. Rev. D* **96**, 064008 (2017), arXiv:1706.03262 [gr-qc].
- [44] J. L. Blázquez-Salcedo, C. F. B. Macedo, V. Cardoso, V. Ferrari, L. Gualtieri, F. S. Khoo, J. Kunz, and P. Pani, *Phys. Rev. D* **94**, 104024 (2016), arXiv:1609.01286 [gr-qc].
- [45] L. Pierini and L. Gualtieri, *Phys. Rev. D* **106**, 104009 (2022), arXiv:2207.11267 [gr-qc].
- [46] J. L. Blázquez-Salcedo, D. D. Doneva, S. Kahlen, J. Kunz, P. Nedkova, and S. S. Yazadjiev, *Phys. Rev. D* **102**, 024086 (2020), arXiv:2006.06006 [gr-qc].
- [47] G. Antoniou, A. Bakopoulos, and P. Kanti, *Phys. Rev. D* **97**, 084037 (2018), arXiv:1711.07431 [hep-th].
- [48] A. Bakopoulos, G. Antoniou, and P. Kanti, *Phys. Rev. D* **99**, 064003 (2019), arXiv:1812.06941 [hep-th].
- [49] F. M. Ramazanoğlu and F. Pretorius, *Phys. Rev. D* **93**, 064005 (2016), arXiv:1601.07475 [gr-qc].

- [50] C. A. R. Herdeiro, E. Radu, N. Sanchis-Gual, and J. A. Font, *Phys. Rev. Lett.* **121**, 101102 (2018), [arXiv:1806.05190 \[gr-qc\]](#).
- [51] F. M. Ramazanoğlu, *Phys. Rev. D* **96**, 064009 (2017), [arXiv:1706.01056 \[gr-qc\]](#).
- [52] F. M. Ramazanoğlu, *Phys. Rev. D* **98**, 044011 (2018), [Erratum: *Phys.Rev.D* 100, 029903 (2019)], [arXiv:1804.00594 \[gr-qc\]](#).
- [53] E. Berti, L. G. Collodel, B. Kleihaus, and J. Kunz, *Phys. Rev. Lett.* **126**, 011104 (2021), [arXiv:2009.03905 \[gr-qc\]](#).
- [54] F. Thaalba, G. Antoniou, and T. P. Sotiriou, *Class. Quant. Grav.* **40**, 155002 (2023), [arXiv:2211.05099 \[gr-qc\]](#).
- [55] T. Regge and J. A. Wheeler, *Phys. Rev.* **108**, 1063 (1957).
- [56] F. J. Zerilli, *Phys. Rev. D* **2**, 2141 (1970).
- [57] C. Gundlach, R. H. Price, and J. Pullin, *Phys. Rev. D* **49**, 883 (1994), [arXiv:gr-qc/9307009](#).
- [58] R. A. Konoplya and A. Zhidenko, *Rev. Mod. Phys.* **83**, 793 (2011), [arXiv:1102.4014 \[gr-qc\]](#).
- [59] W. Boyce and R. DiPrima, *Elementary differential equations and boundary value problems*, 8th ed. (Wiley New York, 2004).
- [60] M. Kimura, *Class. Quant. Grav.* **34**, 235007 (2017), [arXiv:1706.01447 \[gr-qc\]](#).
- [61] M. Kimura and T. Tanaka, *Class. Quant. Grav.* **36**, 055005 (2019), [arXiv:1809.00795 \[gr-qc\]](#).
- [62] J. L. Blázquez-Salcedo, S. Kahlen, and J. Kunz, *Eur. Phys. J. C* **79**, 1021 (2019), [arXiv:1911.01943 \[gr-qc\]](#).
- [63] R. M. Wald, *General Relativity* (Chicago Univ. Pr., Chicago, USA, 1984).
- [64] M. H.-Y. Cheung, K. Destounis, R. P. Macedo, E. Berti, and V. Cardoso, *Phys. Rev. Lett.* **128**, 111103 (2022), [arXiv:2111.05415 \[gr-qc\]](#).
- [65] A. Maselli, S. Yi, L. Pierini, V. Vellucci, L. Reali, L. Gualtieri, and E. Berti, *Phys. Rev. D* **109**, 064060 (2024), [arXiv:2311.14803 \[gr-qc\]](#).